The antiferromagnetic $S = 1/2$ Heisenberg model on the C_{60} fullerene geometry

Roman Rausch[1*,2], Cassian Plorin[3], Matthias Peschke[4]

1 Technische Universität Braunschweig, Institut für Mathematische Physik, Mendelssohnstraße 3, 38106 Braunschweig, Germany
2 Department of Physics, Kyoto University, Kyoto 606-8502, Japan
3 Department of Physics, University of Hamburg, Jungiusstraße 9, D-20355 Hamburg, Germany
4 Institute for Theoretical Physics Amsterdam and Delta Institute for Theoretical Physics, University of Amsterdam, Science Park 904, 1098 XH Amsterdam, The Netherlands
* r.rausch@tu-braunschweig.de

Abstract

We solve the quantum-mechanical antiferromagnetic Heisenberg model with spins positioned on vertices of the truncated icosahedron using the density-matrix renormalization group (DMRG). This describes magnetic properties of the undoped C_{60} fullerene at half filling in the limit of strong on-site interaction U. We calculate the ground state and correlation functions for all possible distances, the lowest singlet and triplet excited states, as well as thermodynamic properties, namely the specific heat and spin susceptibility.

We find that unlike the exactly solvable C_{20} to C_{32}, the lowest excited state is a triplet rather than a singlet, indicating a reduced frustration due to the presence of many hexagon faces and the separation of the pentagon faces. This implies that frustration may be tuneable within the fullerenes by changing their size.

The spin-spin correlations are much stronger along the hexagon bonds and rapidly decrease with distance, so that the molecule is large enough not to be correlated across its whole extent. The specific heat shows a high-temperature peak and a low-temperature shoulder reminiscent of the Kagomé lattice, while the spin susceptibility shows a single broad peak and is very close to the one of C_{20}.

Contents

1 Introduction

The C_{60} buckminsterfullerene molecule, where the 60 carbon atoms sit on the vertices of a truncated icosahedron, is a prominent molecule with a wealth of chemical and nanotechnological applications [1–3], and also of interest in terms of correlated-electron physics. A lattice of C_{60} molecules becomes superconducting when doped with alkali metals [4–7], with a critical temperature of around 40K. This is unusually high for a typical phononic mechanism, so that an electronic mechanism that results from an onsite Hubbard interaction U is under discussion as well [8,9]. At half filling (no doping), a strong U is well-known to cause electron localization via the Mott mechanism and the resulting low-energy properties are described by the antiferromagnetic spin-1/2 Heisenberg model

$$H = J \sum_{\langle ij \rangle} \mathbf{S}_i \cdot \mathbf{S}_j, \tag{1}$$

where $\mathbf{S}_i$ is the spin operator at site i, $J > 0$ is the exchange integral of the order of t^2/U, and t is the hopping integral between nearest-neighbour sites i and j. However, the prototypical Mott systems are transition metal oxides with strong Coulomb repulsion in a narrow d-band, while in carbon atoms, we are dealing with a valence p-band. As a consequence, while the nearest-neighbour hopping parameters are estimated around $2-3$ eV, the Hubbard repulsion U is estimated to be around 9 eV [10–12], which would place the system into the intermediate-coupling range. Still, since solving the full Hubbard model for 60 orbitals on a 2D-like geometry is a hard problem, we may attempt to understand the Heisenberg approximation first. Other authors have argued that there should only be a quantitative difference [12].

Moreover, the C_{60} geometry has an interesting connection to the problem of frustrated spin systems. These arise on geometries like the triangular [13, 14], Kagomé [15–21] or pyrochlore lattice [22], with building blocks of three-site clusters that cannot accommodate antiferromagnetic bonds in a commensurate fashion. The result are spin-liquid states that are disordered and non-trivial. In fullerenes, we instead find 12 pentagon clusters that are also frustrated due to the odd amount of sites, but have no correspondence in the 2D plane, since a tiling by regular pentagons is not possible.

A frustrated spin system is still quite challenging for a theoretical description. For example, the infamous sign problem [23] inhibits an efficient simulation with the Monte Carlo technique. However, tensor-network approaches do not suffer from such a problem. C_{60} is in particular well-suited to a solution using the density-matrix renormalization group (DMRG) [24] due to its finite and very manageable amount of sites.

The truncated icosahedron is part of the icosahedral group I_h, whose other members are the icosahedron with 12 sites and the dodecahedron with 20 sites (which is also the

smallest fullerene C_{20}) [25]. The former has only triangular plaquettes, the latter only pentagonal ones, and both are small enough to be solved exactly by full diagonalization if spatial symmetries are exploited to reduce the Hilbert space size [26]. Small fullerenes up to C_{32} can also be solved exactly [27, 28], but are part of different symmetry groups. Both cases offer a very useful comparison and benchmark.

Each fullerene C_n contains $n/2 - 10$ hexagons and 12 pentagons [29], so that for $n \geq 44$ the number of hexagon faces starts to dominate. For $n \to \infty$, we can expect that the fullerene properties approach those of a hexagonal lattice. But without undertaking the full calculation, it is impossible to say where exactly the crossover happens or what properties might be retained in the large-n limit. In fact, the small fullerenes up to C_{32} do not behave monotonously [27]: For example, the ground state energy for C_{26} and C_{28} is larger than for C_{20} and the first excited state for C_{28} is a triplet instead of a singlet.

In this paper, we present the solution of the Heisenberg model on the C_{60} geometry. Previous works treated the problem classically [12] or approximatively [23], while our calculation is very precise for the ground state. Jiang and Kivelson solved the $t-J$ model on C_{60} [8], which should coincide with our result at half filling. However, they discussed very different questions; and we further present results for the lowest excited states as well as thermodynamics.

Due to two dissimilar types of nearest-neighbour bonds, the corresponding hopping integrals may be slightly different, $t_1 \approx 1.2\ t_2$, leading to different exchange couplings $J_1 \neq J_2$ [12, 30]. For simplicity, we ignore this fact and use a homogeneous $J = J_1 = J_2$ for all bonds. The correlations along the bonds turn out to be nonetheless very different as a consequence of geometry, as will be seen below. We take $J = 1$ as the energy scale, giving all energies in units of J and all temperatures in units of J/k_B, where k_B is the Boltzmann constant.

2 Ground state and correlation functions

2.1 Technical notes

Since DMRG requires a linear chain of sites, we map the C_{60} vertices onto a chain by tracing a Hamilton path through its planar Schlegel graph [8], which creates long-range spin-spin interactions across the chain. Our code incorporates the spin-SU(2) symmetry of the model following Ref. [31], which reduces both the bond dimension of the matrix-product state (MPS) representation of the wavefunction; and the matrix-product operator (MPO) representation of the Hamiltonian. The latter can be further reduced using the lossless compression algorithm of Ref. [32]. It gives only a small benefit of 8% reduction for H itself, with the resulting maximal MPO bond dimension of $\chi(H) = 35 \times 32$ (from 38×35). The benefit for H^2 is larger, yielding $\chi\left(H^2\right) = 564 \times 468$ (reduced from 1444×1225, hence by 55%). With these optimizations, the ground state can be found quite efficiently and we can take the variance per site

$$\Delta E/L = \left(\left\langle H^2 \right\rangle - E^2\right)/L \tag{2}$$

as a global error measure that is immune to local minima.

Interestingly, we find that the number of required subspaces per site in the DMRG simulation is similar to the Heisenberg chain (around 7), but each subspace requires large matrices (with $3500 \sim 4000$ rows/columns, see Tab. 1). This makes the simulation very memory-intensive, requiring several hundreds GB of RAM for good precision.

E	E/L	gap	S_{tot}	$\chi_{\text{SU(2)}}$	$\chi_{\text{sub,SU(2)}}$	χ_{eff}	$\Delta E/L$	GS overlap
-31.131(7)	-0.51886(1)	-	0	10000	3966	43146	$8 \cdot 10^{-5}$	-
-30.775(6)	-0.51292(7)	0.356(0)	1	10000	3770	44302	$1.9 \cdot 10^{-4}$	0
-30.440(9)	-0.50734(9)	0.690(8)	0	10000	3582	46846	$1.6 \cdot 10^{-4}$	$\sim 10^{-8}$

Table 1: Properties of the ground state and the lowest eigenstates: total energy E, energy density E/L, the gap to the ground state, the total spin S_{tot}, the maximal bond dimension of the largest subspace $\chi_{\text{sub,SU(2)}}$ with spin-SU(2) symmetry (the full bond dimension was set to $\chi_{\text{SU(2)}} = 10000$), the effective bond dimension χ_{eff} when not exploiting the symmetry, the variance per site (Eq. 2) and the overlap with the ground state.

2.2 Energy

The ground state lies in the singlet sector with $S_{\text{tot}} = \sum_i \langle \mathbf{S}_i \rangle = 0$ (see Tab. 1). The energy per spin is found to be $E_0/L = -0.51886$. This is lower than the previous result of $E_0/L = -0.50798$ obtained by a spin-wave calculation on top of the classical ground state [23].

Looking at the change in ground-state energy with molecule size, we may compare with C_{20} ($E_0/L = -0.486109$) and C_{32} ($E_0/L = -0.4980$ [27]), and recognize that the value indeed slowly approaches the one for the hexagonal lattice $E_0/L \approx -0.55$ [33]. On the other hand, it is quite close to the much smaller icosahedron ($E_0/L = -0.515657$) which has the same icosahedral symmetry, but only contains triangular plaquettes.

2.3 Correlation functions

The truncated icosahedron is an Archimedean solid, so that all of its sites (vertices) are equivalent; but since two hexagons and one pentagon come together at a vertex, there are two different nearest-neighbour bonds: one that is shared between the two hexagons and two that run between a pentagon and a hexagon (with the total count of 30 and 60, respectively, see Fig. 3 and Fig. 4). We shall call them "hexagon bonds" (H-bonds) and "pentagon bonds" (P-bonds). The wavefunction must respect this geometry, but as the mapping to a chain introduces a bias, this only happens for a sufficiently large bond dimension. Thus, we can average over the respective bonds and take the resulting distribution width as a measure of error, with a δ-distribution expected in the limit of $\chi \to \infty$. Figure 1 shows the result for distances up to $d = 4$, from which we see that for the given bond dimension, the distributions have already become sufficiently δ-like. We obtain $\langle \mathbf{S} \cdot \mathbf{S}_{d=1,H} \rangle = -0.4679$ for the H-bonds and $\langle \mathbf{S} \cdot \mathbf{S}_{d=1,P} \rangle = -0.2849$ for the P-bonds.

For the next-nearest neighbours (distance $d = 2$), there are also two types of bonds (see Fig. 3): two PP-bonds by going along the P-bonds twice, ending up in the same-face pentagon of a given vertex; and four HP-bonds, by going along H and P (in any order), ending up in the same-face hexagon. We find $+0.0581$ for the former, and stronger $+0.1546$ for the latter.

For the third-nearest neighbours (distance $d = 3$), it turns out that there are three types of bonds: The first one connects two sites in the same hexagon (two HPH bonds), and two connect different-face sites (four PPH/HPP bonds and two PHP bonds). For the correlation within the hexagon, we find the largest value -0.1543, for the PHP correlation we find -0.0619 and for the PPH/HPP correlation -0.0496. As the last two lie closely together, they require a very precise ground state to be resolved (see Fig. 1).

We attribute the strong intrahexagon correlation to the hexagons not being frustrated,

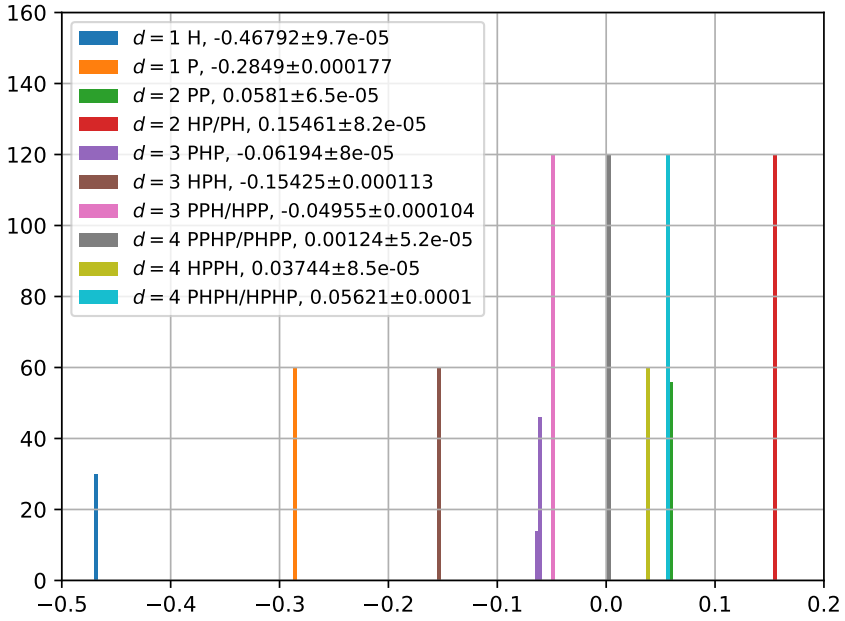

Figure 1: Histogram of the spin-spin correlation function $\langle \mathbf{S} \cdot \mathbf{S}_d \rangle$ in the ground state for distances $d = 1$ to 4 and the various types of C_{60} bonds. For the meaning of the labels, see Fig. 4 and the explanation in the text. The standard deviation of the distribution is taken as the error measure in the legend. The binsize is 0.003.

so that putting a lot of correlation into these bonds can lower the energy more effectively. In fact, the sequence of intrahexagon values is closely matched by the infinite Heisenberg chain [34] or the $L = 6$ Heisenberg ring. On the other hand, the bonds involving pentagons are closely matched by the values of the dodecahedron. Fig. 5 shows a comparison. As a consequence of this, the ground-state energy can actually be naively approximated by taking $E_0 \approx 30 \langle \mathbf{S} \cdot \mathbf{S}_{d=1} \rangle$ [chain] $+ 60 \langle \mathbf{S} \cdot \mathbf{S}_{d=1} \rangle$ [dodecahedron] ≈ -32.739, coming within 95% of the precise DMRG value.

For $d = 4$, the distance is larger than the most distant site in the same-face hexagon. We still find that the largest correlation +0.0562 is found for sites which can be connected via alternating H- and P-bonds (see Fig. 1).

From $d = 5$ onwards, the bond labelling becomes too tedious and we give it up. However, due to sharp distributions we are still able to distinguish the different bonds (see Fig. 2) and find that the trend continues, namely the strongest correlation is found for an alternating H-P path: $\langle \mathbf{S} \cdot \mathbf{S}_{d=5} \rangle = -0.0543$, $\langle \mathbf{S} \cdot \mathbf{S}_{d=6} \rangle = 0.0242$ and $\langle \mathbf{S} \cdot \mathbf{S}_{d=7} \rangle = -0.0244$. For $d = 8$ and $d = 9$, such a path is not possible anymore. Finally, we also note that for $d = 5, 6, 7$ the correlations acquire mixed signs and for $d = 8, 9$ the staggered antiferromagnetic order is flipped, i.e. we have $\langle \mathbf{S} \cdot \mathbf{S}_{d=8} \rangle < 0$ and $\langle \mathbf{S} \cdot \mathbf{S}_{d=9} \rangle > 0$.

Looking at the decay of the correlations with distance, we find $\xi \sim 1.7$ when an exponential fit $\left| \langle \mathbf{S} \cdot \mathbf{S}_d \rangle \right| \sim \exp(-d/\xi)$ is applied to the maximal absolute values (previously, $\xi = 3 \sim 4$ was proposed [23] based on a strong-coupling Quantum Monte Carlo study of the single-band Hubbard model). The icosahedron and dodecahedron have larger excitation gaps, but the maximally possible distance is $d = 3$ and $d = 5$, respectively, so that they are correlated over practically their whole extent (see Fig. 5). For C_{60}, the smallest gap is actually about as large as for the dodecahedron, but the maximal distance is $d = 9$ and the drop-off across the whole molecule is larger. In this sense, the C_{60} spin state is disordered and very different from the ordered Néel phase of the hexagonal lattice [35].

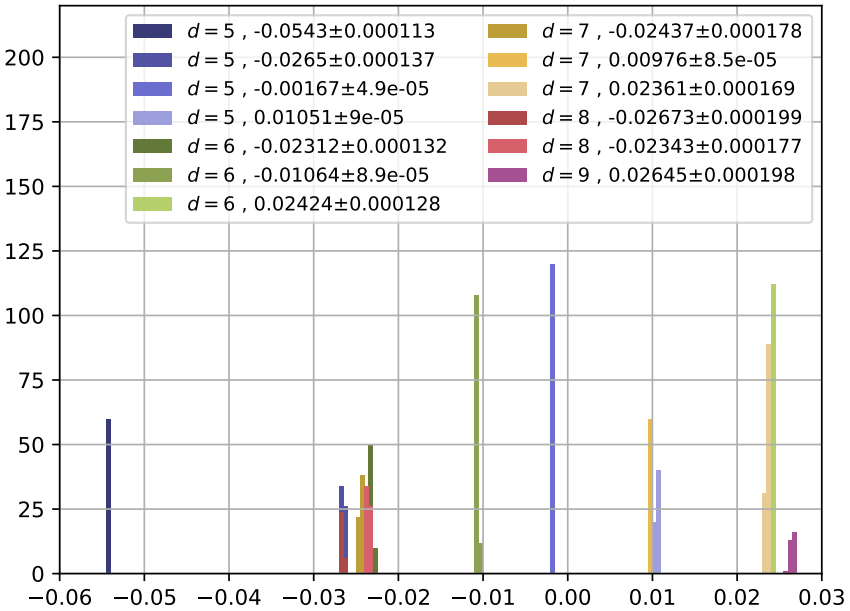

Figure 2: Histogram of the spin-spin correlation function $\langle \mathbf{S} \cdot \mathbf{S}_d \rangle$ in the ground state for distances $d = 5$ to 9 and the various types of C_{60} bonds. The standard deviation of the distribution is taken as the error measure in the legend. The binsize is 0.0005.

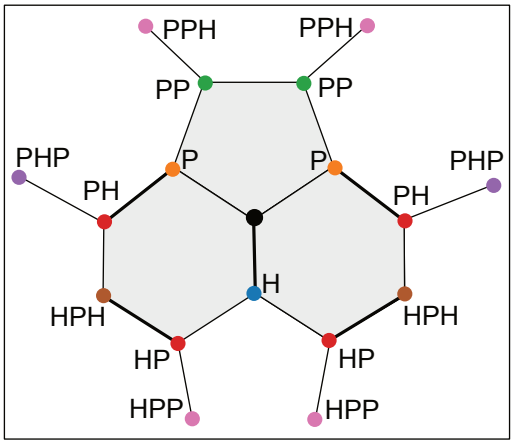

Figure 3: Neighbourhood of a given site (black circle) showing the various types of bonds (cf. Fig 1).

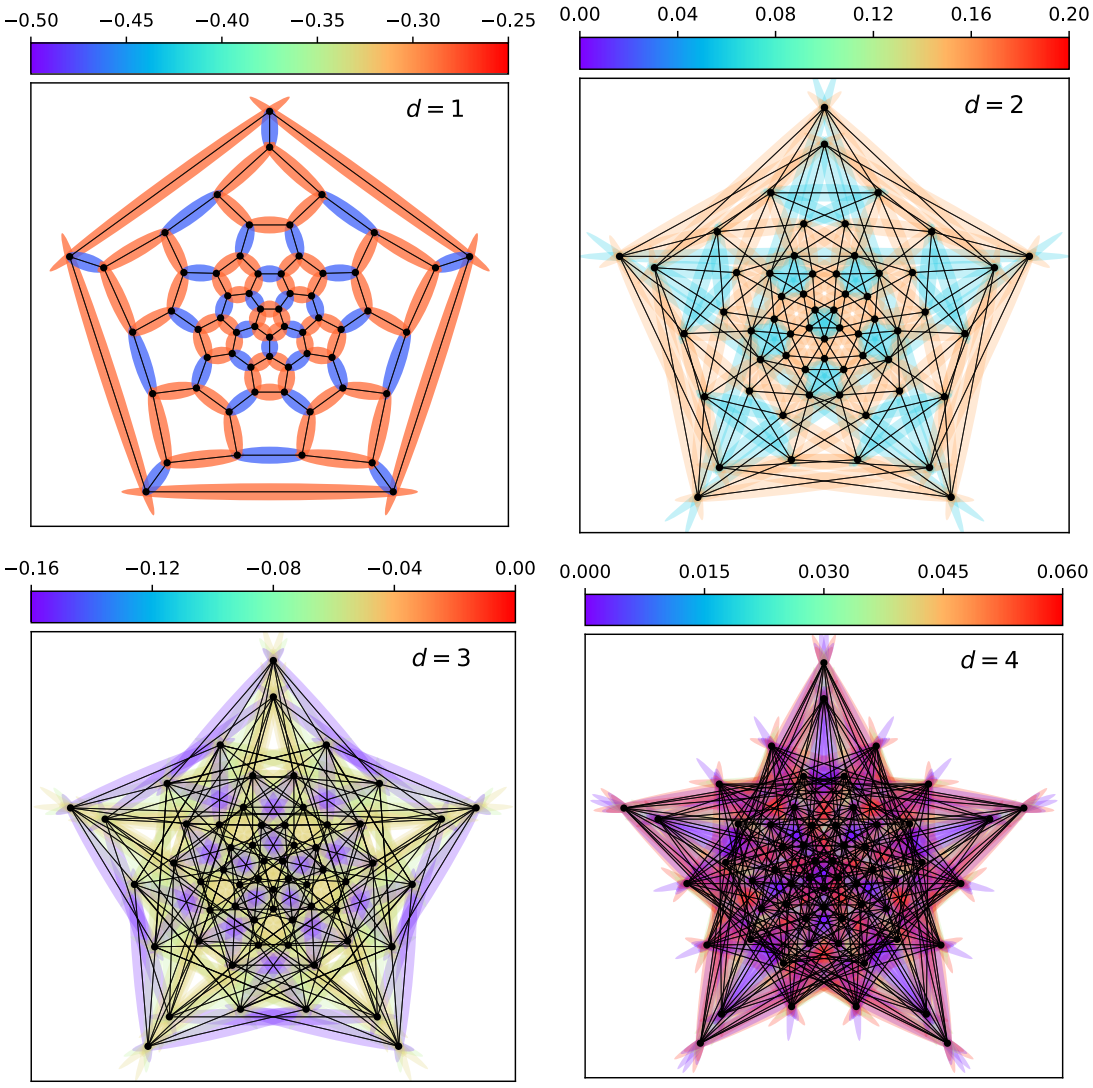

Figure 4: Visualization of the spin-spin correlation function $\langle \mathbf{S} \cdot \mathbf{S}_d \rangle$ in the ground state for distances $d = 1, 2, 3, 4$ in real space on the planar Schlegel projection of C_{60}.

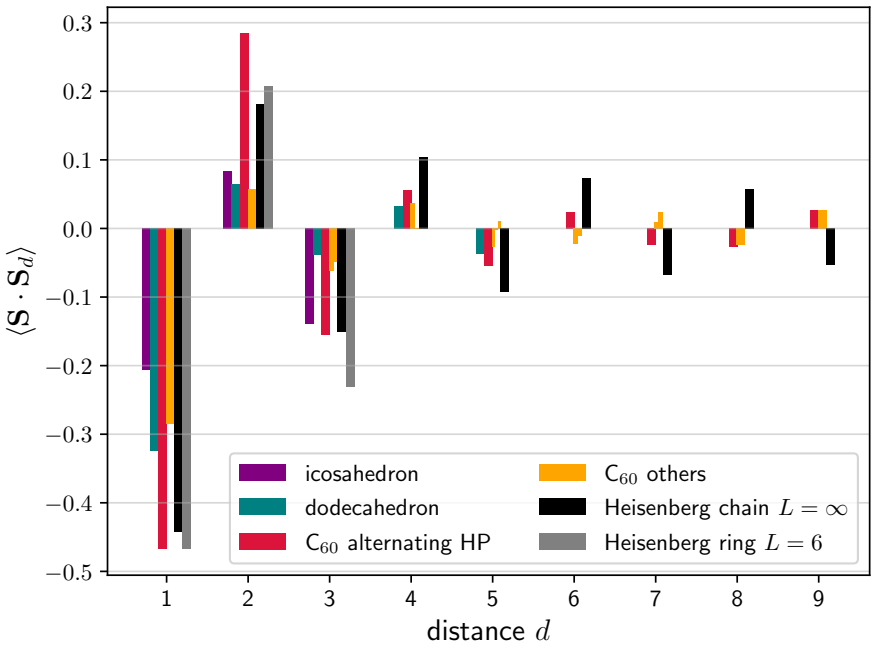

Figure 5: Comparison of the spin-spin correlation function between different geometries: analytical values for the infinite Heisenberg chain [34], the $L = 6$ Heisenberg ring, the icosahedron and the dodecahedron [26]. The C_{60} alternating HP bonds are formed by alternating jumps along H and P (cf. Fig. 3), starting with H; and link two sites within a hexagon up to $d = 3$.

3 Lowest triplet and singlet excitations

By fixing $S_{\text{tot}} = 1$, we can compute the lowest excited state in the triplet sector and look at its properties as well. We limit ourselves to the expectation value of the local spin, $\langle \mathbf{S}_i \rangle$ and the nearest-neighbour correlation functions. The values of $\langle \mathbf{S}_i \rangle$ are shown in Fig. 6. We observe that a good part of the angular momentum (about 60%) localizes on a 20-site ring along a "meridian" of the molecule. As this breaks the spatial symmetry, we conclude that the $S_{\text{tot}} = 1$ is degenerate beyond the three components of the spin projection and the symmetry should be restored when averaging over the whole degenerate subspace. Judging by the low-energy states of other members of the icosahedral group, this points to a $T_{2g,a}$ transformation [26]. The specific position of the 20-site ring must be due to our mapping choice to a chain. In a realistic setting, we expect that the spatial symmetry would in any case be at least slightly broken by the Jahn-Teller effect. In fact, for doped C_{60}, one observes the same preference for a localization of the excess electron along a 20-site ring [36], whereas in our case the same happens to a doped spin (excess angular momentum).

Looking at the nearest-neighbour spin correlations on the left side of Fig. 6, we see that the H-bonds are weakened (-0.468 to -0.414), while the P-bonds are strengthened (-0.2798 to -0.3286) along the 20-site ring as compared to the rest of the system.

A striking property of Heisenberg spins on the icosahedron and dodecahedron geometry [26], as well as for smaller fullerene geometries [27], is that the first excited state is not a triplet, but rather a singlet, a signature of frustration connected to spin-liquid behaviour [15, 37–39]. We therefore calculate the first excited state in the singlet sector ($S_{\text{tot}} = 0$) as the lowest state of the Hamiltonian $\tilde{H} = H + E_p |E_0\rangle\langle E_0|$ with a sufficiently large energy penalty $E_p > 0$ that must be larger than the neutral gap. The result is shown

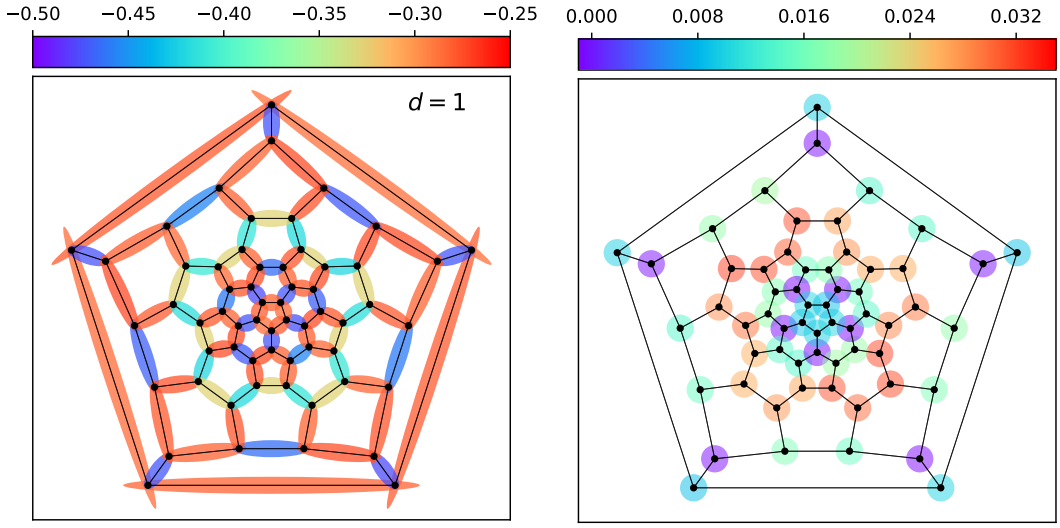

Figure 6: Left: Visualization of the nearest-neighbour spin-spin correlations $\langle \mathbf{S} \cdot \mathbf{S}_{d=1} \rangle$ in the lowest triplet state, $S_{\text{tot}} = 1$. Right: Visualization of the local spin $\langle \mathbf{S}_i \rangle$ in the same state.

in Tab. 1. The neutral gap $\Delta_{S=0} = E_1\left(S_{\text{tot}} = 0\right) - E_0\left(S_{\text{tot}=0}\right) = 0.691$ (cf. icosahedron: 0.533, dodecahedron: 0.316) turns out to be significantly larger than the singlet-triplet gap $\Delta_{S=1} = E_0\left(S_{\text{tot}} = 1\right) - E_0\left(S_{\text{tot}=0}\right) = 0.356$ (cf. icosahedron: 0.900, dodecahedron: 0.519). We attribute this behaviour to the reduced frustration of the C_{60} molecule due to the large amount of hexagonal faces. Furthermore, we note that all the pentagon faces are completely separated by the hexagons, so that all regions with adjacent frustrated pentagons are broken up in C_{60}.

Looking at the spin-spin correlations in the $S_{\text{tot}} = 0$ excited state in Fig. 7, we note that the singlet excitation is also characterized by a 20-site ring with altered correlations, albeit differently positioned. Once again, this indicates degeneracy and comparison within the icosahedral group points to a $H_{g,s}$ representation [26], though this is difficult to prove explicitly using DMRG.

4 Thermodynamics

4.1 Technical notes

We incorporate finite temperatures into the DMRG code using standard techniques [40]. By doubling the degrees of freedom, we go from a description using the wavefunction to a description using the density matrix. This density matrix is again purified into a state vector, but all operators act on the physical sites only, so that the additional "ancilla" cites are automatically traced over when taking expectation values using the state $\left|\beta\right\rangle = \exp\left(-\beta H/2\right)\left|\beta = 0\right\rangle$. The entanglement entropy between the physical sites and the ancillas becomes equal to the thermal entropy. Finally, we can initiate the state at infinite temperature $\beta = 1/T = 0$ by taking the ground state of the entangler Hamiltonian

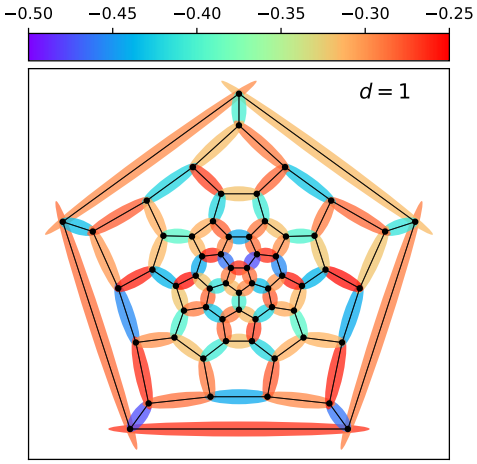

Figure 7: Visualization of the nearest-neighbour spin-spin correlations $\langle \mathbf{S} \cdot \mathbf{S}_{d=1} \rangle$ in the first excited singlet state, $S_{\text{tot}} = 0$. Note the 20-site ring of altered correlations in the lower part.

$$H_{\beta=0} = \sum_i \mathbf{S}_i \cdot \mathbf{S}_{a(i)}, \tag{3}$$

where $a\,(i)$ indicates the ancilla site attached to the physical site i.

We then apply a propagation in β using the 2-site TDVP (time-dependent variational principle) algorithm [41] with the step size of $d\beta = 0.1$. This allows to grow the bond dimension dynamically, until it becomes prohibitively large, at which point we switch to the faster 1-site algorithm (typically around $\beta = 6 - 10$). To strike a balance between accuracy and running time, we limit the bond dimension per subspace to $\chi_{\text{loc}} \sim 200 - 800$, rather than limiting the total bond dimension. This ensures that the largest matrix is at most $\chi_{\text{loc}} \times \chi_{\text{loc}}$ and the duration of the remaining propagation can be estimated. A benchmark of this approach for the exactly solvable C_{20} is given in Appendix A. Finally, there is a technical question of whether to incorporate the ancillas as separate sites (with the cost of longer-ranged hopping) or as "super-sites" [40]. We take the super-site approach for better accuracy.

The relevant quantities are the partition function

$$Z_\beta = \langle \beta | \beta \rangle, \tag{4}$$

the internal energy

$$E\,(\beta) = \langle H \rangle_\beta = Z_\beta^{-1} \langle \beta | H | \beta \rangle, \tag{5}$$

the specific heat per site (or per spin):

$$c\,(T) = \frac{C\,(T)}{L} = \frac{1}{L}\frac{\partial E}{\partial T} = \frac{1}{L}\beta^2 \big[\langle H^2 \rangle_\beta - \langle H \rangle_\beta^2 \big], \tag{6}$$

and the zero-field uniform magnetic susceptibility

$$\chi = \frac{1}{L} \lim_{\mathbf{B}\to 0} \nabla_{\mathbf{B}} \cdot \mathbf{M} = \frac{1}{L}\beta \big[\langle \mathbf{S}^2 \rangle_\beta - \langle \mathbf{S} \rangle_\beta^2 \big], \tag{7}$$

where $\mathbf{M}$ is the magnetization at a given external field strength $\mathbf{B}$ and the Hamiltonian is changed to $H \to H - \mathbf{B} \cdot \mathbf{S}$, with the total spin $\mathbf{S}$:

$$\mathbf{M} = \langle \mathbf{S} \rangle_{\mathbf{B},\beta} = Z_{\mathbf{B},\beta}^{-1} \langle \beta = 0 | \mathbf{S}\ e^{-\beta(H - \mathbf{B}\cdot\mathbf{S})} | \beta = 0 \rangle. \tag{8}$$

While the specific heat can be exactly calculated using the squared Hamiltonian average $\langle H^2 \rangle_\beta$, in practice this becomes quite expensive at every β-step, so that we use a numerical differentiation of $E(\beta)$ with spline interpolation instead.

4.2 Specific heat

The result for $c(T)$ is shown in Fig. 8. All members of the icosahedral group exhibit a two-peak structure: The icosahedron shows a high-T shoulder and a low-T peak. The dodecahedron has two peaks. For C_{60}, we find instead a high-T peak (around $T \sim 0.58$) and low-T shoulder (around $T \sim 0.15 - 0.19$). The high-T peak can be attributed to the energy scale given by $J = 1$ and is a general feature of Heisenberg chains [40, 42, 43]. The low-T peak can be attributed to the second scale of the energy gap, provided that the states are well separated.

We recall that for a two-level system given by the Hamiltonian $H = \mathrm{diag}(0, \Delta)$, the specific heat has a Schottky peak at $T/\Delta \approx 0.417$. In other words, a maximum appears when the temperature is tuned to the gap Δ. This is roughly consistent with the gap values given in Tab. 1. The fact that we have a shoulder rather than a clear peak implies that several states of close energy contribute to $c(T)$, i.e. a comparatively high density of states close to the first excited state. In fact, we can see that as the bond dimension in the DMRG calculation is increased, we are able to better describe the low-lying states, leading to a flattening of a very shallow peak to a shoulder.

We note that the form of the specific heat for C_{60} is quite close in shape to what is found for the Heisenberg model on the Kagomé lattice [15–17]. However, the latter has a much smaller singlet-triplet gap of 0.13 and a very small neutral gap of ~ 0.05 [19, 20], resulting in a low-energy shoulder or shallow peak, whose exact position is difficult to pinpoint, but seems to be below $T \sim 0.05$ [17]. Since the Kagomé lattice has hexagons and frustrated triangles as faces, compared to the frustrated pentagons and hexagons of C_{60}, we may have a similarity in the eigenvalue distributions. See also the comparison of the Kagomé lattice to a cuboctahedron [43].

4.3 Spin susceptibilty

Fig. 9 shows the result for the susceptibility $\chi(T)$. It can be interpreted in a similar way, the difference being that singlet states do not contribute anymore. Moreover, it is easy to show that for high temperatures, $\chi(T)$ follows a universal Curie law $\chi(T) \sim 3/4 \cdot T^{-1}$, while for $T \to 0$ we expect $\chi \to 0$, since the ground state is a spin singlet and not susceptible to small fields. In between, $\chi(T)$ should have at least one peak. We observe that it is positioned at a higher temperature for the icosahedron due to the larger singlet-triplet gap. The dodecahedron and C_{60}, on the other hand, are remarkably close, though $\chi(T)$ is always slightly larger for C_{60} and does not go to zero as fast for very small temperatures, which we ascribe to the small singlet-triplet gap.

5 Conclusion

We have presented a solution of the Heisenberg model on the C_{60} fullerene geometry. The spin-spin correlations in the ground state can be determined very accurately using DMRG

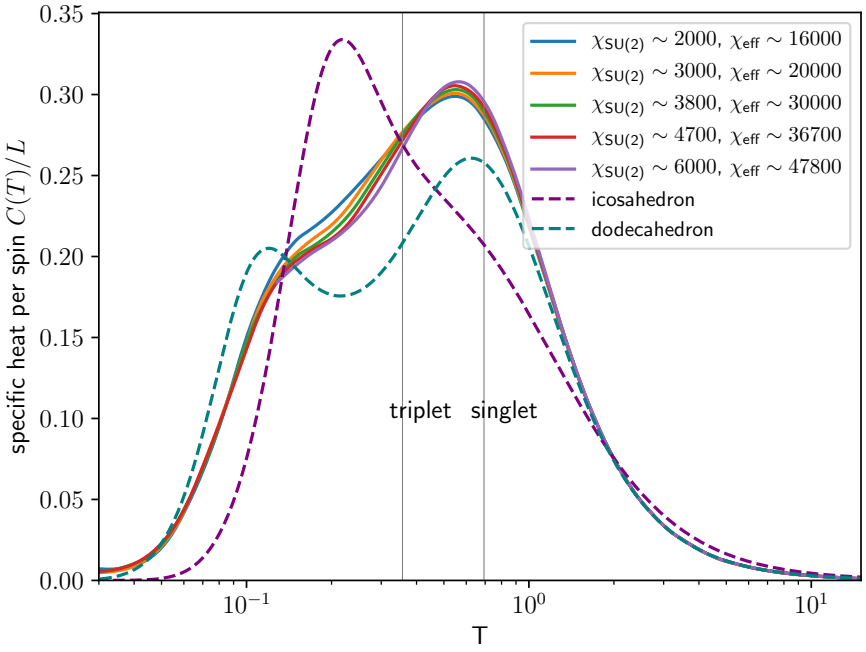

Figure 8: Specific heat of C_{60} for different bond dimensions (Eq. 6). The bond dimension per subspace was limited to $\chi_{\text{loc}} = 300, 400, 500, 600, 800$. The grey vertical lines indicate the triplet and singlet gaps with respect to the ground state.

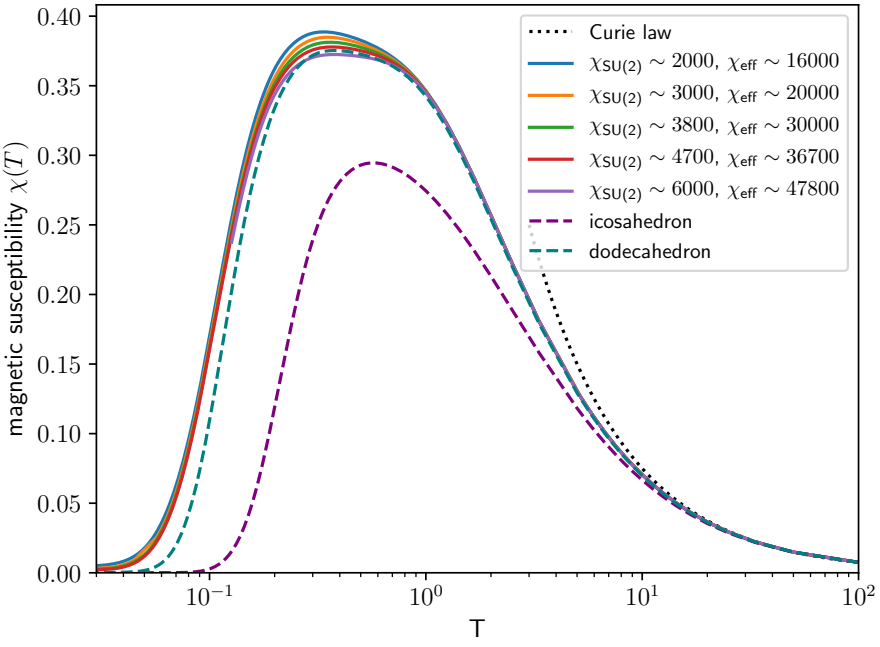

Figure 9: Zero-field uniform magnetic susceptibility C_{60} (Eq. 7) for different bond dimensions. Parameters as in Fig. 8.

and indicate that the C_{60} molecule is large enough not to be fully correlated across its full extent. The strongest correlations are found along an alternating path of hexagon and pentagon bonds, a consequence of the fact that the hexagons are not frustrated. Furthermore, for large distances, we find a deviation from the staggered sign pattern of an antiferromagnet.

Most strikingly (and unlike smaller fullerenes), the first excited state is a triplet and not a singlet, indicating weaker frustration. This can be attributed to the large number of unfrustrated hexagon faces which separate all the pentagon faces from each other, suggesting that frustration is tuneable in small fullerenes as a function of their size. Still, we find that the ground state of C_{60} is disordered with a very short correlation length of $\xi \sim 1.7$ and therefore quite dissimilar from the ordered Néel state of the hexagonal lattice.

In terms of thermodynamics, we find a two-peak structure of the specific heat, similar to what is found for the dodecahedron or the Kagomé lattice, but the low-temperature feature is very shallow for C_{60} (a shoulder). The spin susceptibility shows a broad peak very similar to the dodecahedron, but approaches zero less rapidly for $T \to 0$.

We have not attempted to find out the spatial symmetry transformations of the lowest eigenstates, but educated guesses can be made by comparing with the icosahedron and dodecahedron. Neither have we studied the effect of a strong external field. Another open question is whether the frustrated pentagons can still measurably affect any properties of C_n in the large-n limit. DMRG is well equipped to answer these questions and solve the Heisenberg model for even larger n, or for fullerene dimers [44]. Another system that is well-suited for DMRG is the encapsulation of magnetic rare-earth atoms by fullerenes or fullerene-like molecules [45, 46], simulated by the Heisenberg model.

Acknowledgements

Funding information R.R. thanks the Japan Society for the Promotion of Science (JSPS) and the Alexander von Humboldt Foundation. Computations were performed at the PHYSnet computation cluster at Hamburg University. R.R. gratefully acknowledges support by JSPS, KAKENHI Grant No. JP18F18750. C.P. is supported by the Deutsche Forschungsgemeinschaft (DFG) through the Cluster of Excellence Advanced Imaging of Matter – EXC 2056 – project ID 390715994. M.P. has received funding from the European Research Council (ERC) under the European Union's Horizon 2020 research and innovation programme (Grant Agreement No. 677061).

A Specific heat of C_{20}

As a benchmark of the thermal DMRG algorithm, we calculate the specific heat of the dodecahedron (C_{20}) and show the results in Fig. 10. While the ground state offers no challenge for DMRG and converges in a matter of seconds, the β-propagation is more demanding and we see that a high bond dimension is required to get the precise location and height of the low-temperature peak. However, even smaller bond dimensions are able to qualitatively capture the two-peak structure. The implication for C_{60} is that while we cannot claim that the results are numerically exact, since a much higher bond dimension may be required to achieve such precision, we expect that the qualitative behaviour should be captured as well.

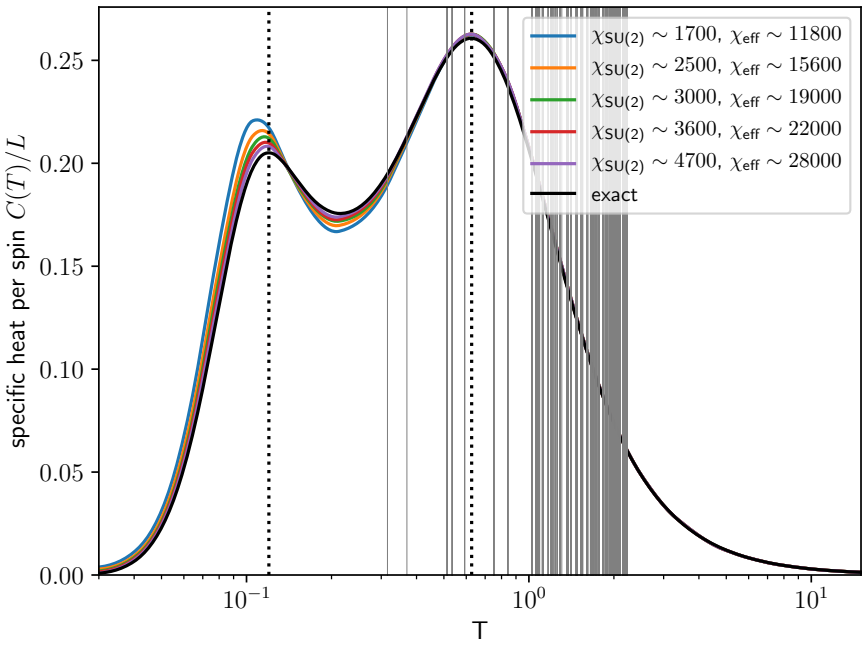

Figure 10: Specific heat of C_{20} for different bond dimensions. The bond dimension per subspace was limited to $\chi_{\text{loc}} = 300, 400, 500, 600, 800$. The grey vertical lines indicate the first 1000 eigenenergies relative to the ground state, $E_n - E_0$. The dotted vertical lines indicate the peak positions from Ref. [26]. To obtain the exact result, we used the Kernel Polynomial Method [47] with 1000 lowest eigenstates, 1000 Chebyshev moments and 1000 random vectors.

References

[1] A. J. Stace and P. O'Brien, *Fullerenes: past, present and future, celebrating the 30th anniversary of buckminster fullerene* (2016).

[2] S. C. Benjamin, A. Ardavan, G. A. D. Briggs, D. A. Britz, D. Gunlycke, J. Jefferson, M. A. G. Jones, D. F. Leigh, B. W. Lovett, A. N. Khlobystov, S. A. Lyon, J. J. L. Morton *et al.*, *Towards a fullerene-based quantum computer*, Journal of Physics: Condensed Matter **18**(21), S867 (2006), doi:10.1088/0953-8984/18/21/s12.

[3] C. B. Winkelmann, N. Roch, W. Wernsdorfer, V. Bouchiat and F. Balestro, *Superconductivity in a single-c60 transistor*, Nature Physics **5**(12), 876 (2009).

[4] A. Hebard, M. Rosseinsky, R. Haddon, D. Murphy, S. Glarum, T. Palstra, A. Ramirez and A. Kortan, *Superconductivity at 18k in potassium-doped c60*, Nature **350**(6319), 600 (1991).

[5] T. Palstra, O. Zhou, Y. Iwasa, P. Sulewski, R. Fleming and B. Zegarski, *Superconductivity at 40k in cesium doped c60*, Solid State Communications **93**(4), 327 (1995), doi:https://doi.org/10.1016/0038-1098(94)00787-X.

[6] Y. Takabayashi and K. Prassides, *Unconventional high-T_c superconductivity in fullerides*, Philosophical Transactions of the Royal Society A: Mathematical, Physical and Engineering Sciences **374**(2076), 20150320 (2016).

[7] M. Kim, Y. Nomura, M. Ferrero, P. Seth, O. Parcollet and A. Georges, *Enhancing superconductivity in A_3c_{60} fullerides*, Phys. Rev. B **94**, 155152 (2016), doi:10.1103/PhysRevB.94.155152.

[8] H.-C. Jiang and S. Kivelson, *Electronic pair binding and hund's rule violations in doped c_{60}*, Phys. Rev. B **93**, 165406 (2016), doi:10.1103/PhysRevB.93.165406.

[9] F. Lin, E. S. Sørensen, C. Kallin and A. J. Berlinsky, *Strong correlation effects in the fullerene c_{20} studied using a one-band hubbard model*, Phys. Rev. B **76**, 033414 (2007), doi:10.1103/PhysRevB.76.033414.

[10] S. Chakravarty, M. P. Gelfand and S. Kivelson, *Electronic correlation effects and superconductivity in doped fullerenes*, Science **254**(5034), 970 (1991), doi:10.1126/science.254.5034.970, `https://science.sciencemag.org/content/254/5034/970.full.pdf`.

[11] G. Stollhoff, *Anomalous electron-lattice coupling in c_{60}*, Phys. Rev. B **44**, 10998 (1991), doi:10.1103/PhysRevB.44.10998.

[12] D. Coffey and S. A. Trugman, *Magnetic properties of undoped c_{60}*, Phys. Rev. Lett. **69**, 176 (1992), doi:10.1103/PhysRevLett.69.176.

[13] Z. Zhu and S. R. White, *Spin liquid phase of the $s = \frac{1}{2}$ $J_1 - J_2$ heisenberg model on the triangular lattice*, Phys. Rev. B **92**, 041105 (2015), doi:10.1103/PhysRevB.92.041105.

[14] P. Prelovsek and J. Kokalj, *Finite-temperature properties of the extended heisenberg model on a triangular lattice*, Phys. Rev. B **98**, 035107 (2018), doi:10.1103/PhysRevB.98.035107.

[15] P. Sindzingre, G. Misguich, C. Lhuillier, B. Bernu, L. Pierre, C. Waldtmann and H.-U. Everts, *Magnetothermodynamics of the spin- $\frac{1}{2}$ kagomé antiferromagnet*, Phys. Rev. Lett. **84**, 2953 (2000), doi:10.1103/PhysRevLett.84.2953.

[16] G. Misguich and B. Bernu, *Specific heat of the $s = \frac{1}{2}$ heisenberg model on the kagome lattice: High-temperature series expansion analysis*, Phys. Rev. B **71**, 014417 (2005), doi:10.1103/PhysRevB.71.014417.

[17] G. Misguich and P. Sindzingre, *Magnetic susceptibility and specific heat of the spin-1/2 heisenberg model on the kagome lattice and experimental data on zncu3(oh)6cl2*, The European Physical Journal B **59**(3), 305 (2007).

[18] H. C. Jiang, Z. Y. Weng and D. N. Sheng, *Density matrix renormalization group numerical study of the kagome antiferromagnet*, Phys. Rev. Lett. **101**, 117203 (2008), doi:10.1103/PhysRevLett.101.117203.

[19] S. Yan, D. A. Huse and S. R. White, *Spin-liquid ground state of the s = 1/2 kagome heisenberg antiferromagnet*, Science **332**(6034), 1173 (2011), doi:10.1126/science.1201080, `https://science.sciencemag.org/content/332/6034/1173.full.pdf`.

[20] S. Depenbrock, I. P. McCulloch and U. Schollwöck, *Nature of the spin-liquid ground state of the $s = 1/2$ heisenberg model on the kagome lattice*, Phys. Rev. Lett. **109**, 067201 (2012), doi:10.1103/PhysRevLett.109.067201.

[21] J.-W. Mei, J.-Y. Chen, H. He and X.-G. Wen, *Gapped spin liquid with z2 topological order for the kagome heisenberg model*, Phys. Rev. B **95**, 235107 (2017), doi:10.1103/PhysRevB.95.235107.

[22] R. Schäfer, I. Hagymási, R. Moessner and D. J. Luitz, *The pyrochlore s=1/2 heisenberg antiferromagnet at finite temperature*, arXiv preprint arXiv:2003.04898 (2020).

[23] R. T. Scalettar, A. Moreo, E. Dagotto, L. Bergomi, T. Jolicoeur and H. Monien, *Ground-state properties of the hubbard model on a c_{60} cluster*, Phys. Rev. B **47**, 12316 (1993), doi:10.1103/PhysRevB.47.12316.

[24] U. Schollwöck, *The density-matrix renormalization group in the age of matrix product states*, Annals of Physics **326**(1), 96 (2011), doi:https://doi.org/10.1016/j.aop.2010.09.012, January 2011 Special Issue.

[25] H. Fripertinger, *The cycle index of the symmetry group of the fullerene c60*, Match (Mulheim an der Ruhr, Germany) **33**, 121 (1996).

[26] N. P. Konstantinidis, *Antiferromagnetic heisenberg model on clusters with icosahedral symmetry*, Phys. Rev. B **72**, 064453 (2005), doi:10.1103/PhysRevB.72.064453.

[27] N. P. Konstantinidis, *$s = \frac{1}{2}$ antiferromagnetic heisenberg model on fullerene-type symmetry clusters*, Phys. Rev. B **80**, 134427 (2009), doi:10.1103/PhysRevB.80.134427.

[28] N. A. Modine and E. Kaxiras, *Variational hilbert-space-truncation approach to quantum heisenberg antiferromagnets on frustrated clusters*, Phys. Rev. B **53**, 2546 (1996), doi:10.1103/PhysRevB.53.2546.

[29] P. W. Fowler and D. Manolopoulos, *An Atlas of Fullerenes*, Courier Corporation (2007).

[30] V. Elser and R. Haddon, *Icosahedral c60: an aromatic molecule with a vanishingly small ring current magnetic susceptibility*, Nature **325**(6107), 792 (1987).

[31] I. P. McCulloch, *From density-matrix renormalization group to matrix product states*, Journal of Statistical Mechanics: Theory and Experiment **2007**(10), P10014 (2007), doi:10.1088/1742-5468/2007/10/p10014.

[32] C. Hubig, I. P. McCulloch and U. Schollwöck, *Generic construction of efficient matrix product operators*, Phys. Rev. B **95**, 035129 (2017), doi:10.1103/PhysRevB.95.035129.

[33] H. C. Jiang, Z. Y. Weng and T. Xiang, *Accurate determination of tensor network state of quantum lattice models in two dimensions*, Phys. Rev. Lett. **101**, 090603 (2008), doi:10.1103/PhysRevLett.101.090603.

[34] J. Sato, M. Shiroishi and M. Takahashi, *Correlation functions of the spin-1/2 antiferromagnetic heisenberg chain: Exact calculation via the generating function*, Nuclear Physics B **729**(3), 441 (2005), doi:https://doi.org/10.1016/j.nuclphysb.2005.08.045.

[35] R. Ganesh, J. van den Brink and S. Nishimoto, *Deconfined criticality in the frustrated heisenberg honeycomb antiferromagnet*, Phys. Rev. Lett. **110**, 127203 (2013), doi:10.1103/PhysRevLett.110.127203.

[36] V. Brouet, H. Alloul, S. Gàràj and L. Forro, *Nmr studies of insulating, metallic, and superconducting fullerides: Importance of correlations and jahn–teller distortions*, In *Fullerene-Based Materials*, pp. 165–199. Springer (2004).

[37] R. R. P. Singh and D. A. Huse, *Triplet and singlet excitations in the valence bond crystal phase of the kagome lattice heisenberg model*, Phys. Rev. B **77**, 144415 (2008), doi:10.1103/PhysRevB.77.144415.

[38] A. M. Läuchli, J. Sudan and R. Moessner, *$s = \frac{1}{2}$ kagome heisenberg antiferromagnet revisited*, Phys. Rev. B **100**, 155142 (2019), doi:10.1103/PhysRevB.100.155142.

[39] P. Prelovsek, K. Morita, T. Tohyama and J. Herbrych, *Vanishing wilson ratio as the hallmark of quantum spin-liquid models*, Phys. Rev. Research **2**, 023024 (2020), doi:10.1103/PhysRevResearch.2.023024.

[40] A. E. Feiguin and S. R. White, *Finite-temperature density matrix renormalization using an enlarged hilbert space*, Phys. Rev. B **72**, 220401 (2005), doi:10.1103/PhysRevB.72.220401.

[41] J. Haegeman, C. Lubich, I. Oseledets, B. Vandereycken and F. Verstraete, *Unifying time evolution and optimization with matrix product states*, Phys. Rev. B **94**, 165116 (2016), doi:10.1103/PhysRevB.94.165116.

[42] T. Xiang, *Thermodynamics of quantum heisenberg spin chains*, Phys. Rev. B **58**, 9142 (1998), doi:10.1103/PhysRevB.58.9142.

[43] H.-J. Schmidt, A. Hauser, A. Lohmann and J. Richter, *Interpolation between low and high temperatures of the specific heat for spin systems*, Phys. Rev. E **95**, 042110 (2017), doi:10.1103/PhysRevE.95.042110.

[44] N. P. Konstantinidis, *Ground state magnetic response of two coupled dodecahedra*, Journal of Physics: Condensed Matter **28**(1), 016001 (2015), doi:10.1088/0953-8984/28/1/016001.

[45] X. Lu, T. Akasaka and S. Nagase, *Rare earth metals trapped inside fullerenes–endohedral metallofullerenes (emfs)*, Rare Earth Coordination Chemistry: Fundamentals and Applications pp. 273–307 (2010).

[46] J. Wang, Y. Liu and Y.-C. Li, *Magnetic silicon fullerene*, Physical Chemistry Chemical Physics **12**(37), 11428 (2010).

[47] A. Weiße, G. Wellein, A. Alvermann and H. Fehske, *The kernel polynomial method*, Rev. Mod. Phys. **78**, 275 (2006), doi:10.1103/RevModPhys.78.275.